Electronic structure and spin-to-charge conversion in the chalcopyrite $CdGeAs_2$

N. Tarakameh Samani*,[1,2] F. Scali*,[1] C. Zucchetti,[1] N. Mignani,[1] F. Mazzola,[3] I. Vobornik,[4] J. Fujii,[4] K. Raju,[5,6] S. Mani,[5,6] R. Sankar,[5,6] M. Puppin,[7] F. Ciccacci,[1] M. Finazzi,[1] E. Carpene,[2] C. Dallera,[1] F. Bottegoni,[1] and A. Crepaldi[1,2,*]

[1]*Dipartimento di Fisica, Politecnico di Milano, Piazza Leonardo da Vinci 32, Milan 20133, Italy*
[2]*IFN-CNR, Dipartimento di Fisica, Politecnico di Milano, Piazza Leonardo da Vinci 32, Milan 20133, Italy*
[3]*Department of Physics and Astronomy 'Galileo Galilei', University of Padova, Via Marzolo 8, Padova 35131, Italy*
[4]*CNR-Istituto Officina dei Materiali (CNR-IOM), Strada Statale 14, km 163.5, 34149 Trieste, Italy*
[5]*Institute of Physics, Academia Sinica, Nankang, Taipei R.O.C. Taiwan 11529*
[6]*Center for Condensed Matter Sciences, National Taiwan University, Taipei 10617, Taiwan*
[7]*Institute of Physics, École Polytechnique Fédérale de Lausanne (EPFL), CH-1015 Lausanne, Switzerland*

(Dated: March 16, 2026)

Ternary semiconductors with chalcopyrite structure are of growing interest for electronic, energy-conversion, and spintronic applications. Using angle-resolved photoemission spectroscopy, we directly map the band structure of $CdGeAs_2$, the prototypical chalcopyrite described by a modified Kane model that predicts the coexistence of flat bands and highly dispersive linear states. The combined effect of tetragonal distortion and broken inversion symmetry reduces the band degeneracy, allowing us to resolve three distinct states at the top of the valence band, with band velocities comparable to those reported in Dirac semimetals. We further probe the spin-to-charge conversion properties of $CdGeAs_2$ by optically injecting spin-polarized carriers and detecting the resulting inverse spin Hall effect (ISHE). The photon-energy dependence of the ISHE signal and theoretical calculations of the optically injected spin polarization allow us to identify the specific valence-to-conduction transitions responsible for net spin accumulation and to estimate the spin diffusion length. These results demonstrate that chalcopyrite semiconductors provide a versatile platform for opto-spintronics.

I. INTRODUCTION

The family of chalcopyrite ternary compounds ABC_2 comprises more than fifty semiconductors with highly tunable crystal and electronic structures, giving rise to a wide variety of physical properties [1–5]. Over the years, chalcopyrites have been widely studied for their large photovoltaic conversion efficiency [6, 7], high thermoelectric performance [4], and bulk photovoltaic effect [8], making them a unique platform for multifunctional energy conversion [9]. Structurally, they can be described as distorted zinc-blende crystals in which the tetragonal crystal field lifts the zone-center degeneracy between the heavy- and light-hole bands. This effect can be exploited to generate photoelectrons with spin polarization approaching 100% [10].

The coexistence of bands with very different effective masses underlies many of these intriguing properties. In particular, the light-hole band exhibits linear dispersion and high carrier mobilities. Figure 1(a) illustrates this distinctive feature through a solution of the Kildal model, an extension of the Kane Hamiltonian [11] that incorporates the anisotropic crystal field to describe the low-energy states near the band gap [12]. In chalcopyrites, Kane electrons can emerge as three-dimensional massless charge carriers originating from a nearly vanishing band-gap, where linearly dispersing states (in blue-green in Fig. 1) intersect a flat heavy-hole band (pink) near the Γ point[13, 14]. The band degeneracy can be tuned by hydrostatic pressure [15] or by chemical composition, with the gap-closing point marking the boundary between a trivial semiconductor and a three-dimensional topological insulator [2]. Beyond its electronic structure, $CdGeAs_2$ is notable for its nonlinear optical properties [16]. Its broad transparency window (2.4–18 μm) combined with a large nonlinear optical coefficient [17, 18] makes it an attractive material for mid-infrared frequency conversion [19, 20].

In this work, we present an angle-resolved photoemission spectroscopy (ARPES) study of the electronic structure of $CdGeAs_2$, the archetypal chalcopyrite originally modeled by Kildal [12]. We resolve three distinct states forming the top of the valence band: two with linear dispersion, displaying band velocities of $\sim 1.3 \times 10^6$ and $\sim 0.5 \times 10^6$ m/s, and a third, flatter band well described by a parabolic dispersion with an effective mass of $\sim 1.1\, m_e$ (with m_e the free-electron mass). The bulk inversion asymmetry is expected to lift the spin degeneracy of the bands near the Γ point, we therefore investigate how this unique spin-polarized electronic structure influence the spin-to-charge interconversion properties by measuring the photon-energy dependence of the inverse spin Hall effect (ISHE) signal, which originates from spin-dependent scattering of optically injected spins in $CdGeAs_2$. Comparison with theoretical models of valence and conduction band spin polarization as a function of photon energy suggests that the ISHE spectrum can be captured by a simple diffusion model that accounts for the photon-energy dependence of the spin-injection rate. Taken together, the results establish $CdGeAs_2$ as a promising semiconductor platform for opto-spintronics applications.

II. EXPERIMENTAL DETAILS

High-quality $CdGeAs_2$ single crystals are grown by chemical vapor transport using bromine as the transport agent, a

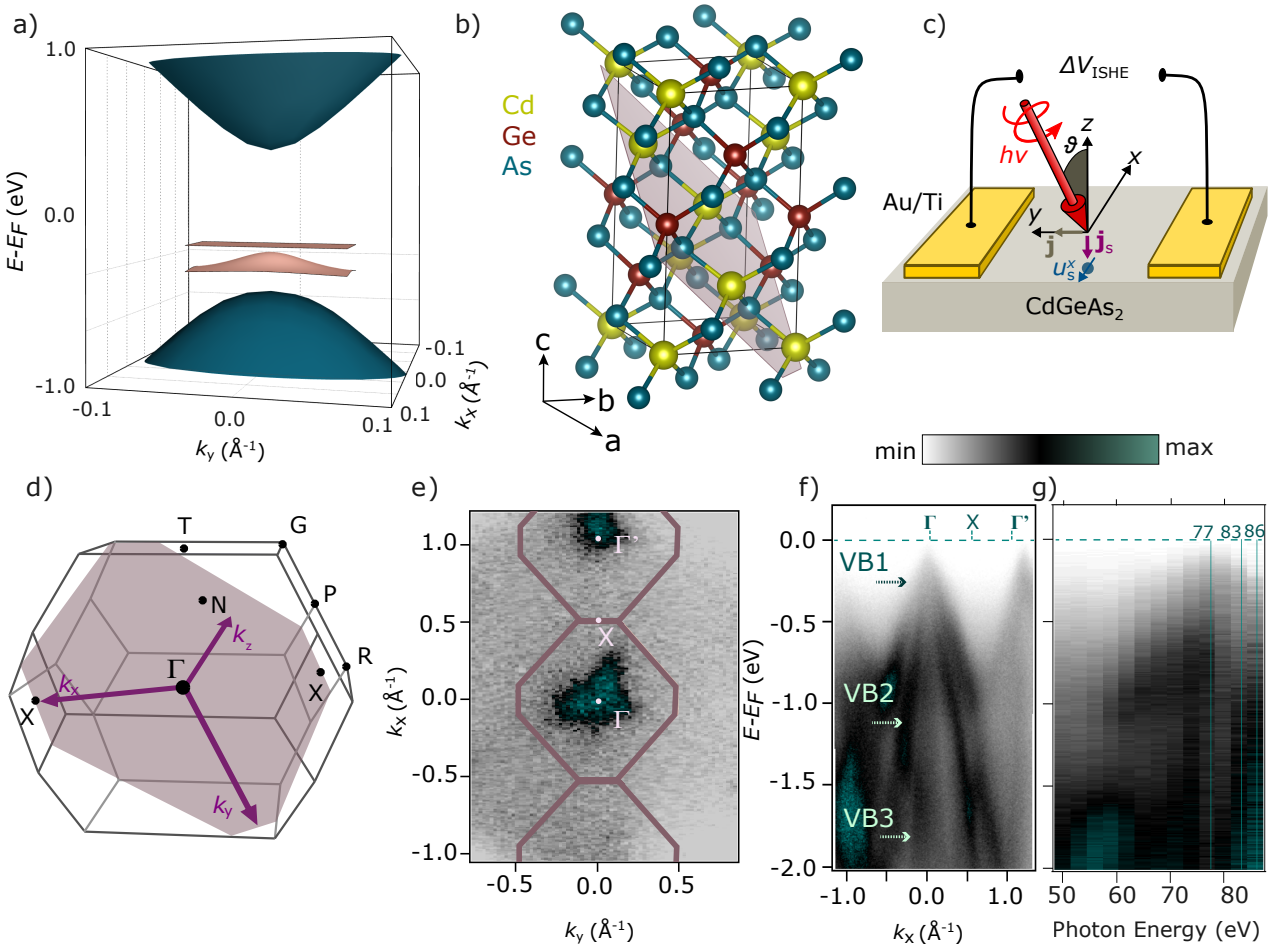

FIG. 1 (a) Schematic band dispersions near the fundamental gap of a chalcopyrite, obtained from the Kildal model. Pink and blue-green colors indicate flat and dispersive states, respectively. (b) Crystal structure of $CdGeAs_2$ with Cd (yellow), Ge (red) and As (blue-green) with diamond-like coordination. Black line traces the conventional tetragonal cell and the red area highlights the intersection with a plane parallel to the surface termination. (c) Sketch of the ISHE geometry, with two Au/Ti ohmic pads deposited on top of a $4 \times 2\,\mathrm{mm}^2$-wide and 1 mm-thick $CdGeAs_2$ sample; circularly polarized light beam illuminates the sample at polar angle ϑ with respect to the sample normal in the xz-plane. u_p^x is the detected x-axis component of the spin polarization unit vector, $\mathbf{j}_s$ the spin current density, and $\mathbf{j}_c$ the charge current density. (d) Bulk Brillouin zone corresponding to the body-centered tetragonal primitive cell, labels indicate the high-symmetry points along with the convention adopted in the manuscript to indicate (k_x, k_y, k_z). (e) Constant energy map acquired at $E - E_F = -200$ meV with 72.5 eV photon energy. The Γ, X and Γ′ points are shown along with the BZ for $k_z = 0\,\text{Å}^{-1}$, corresponding to the red plane shown in panel (d). (f) band dispersion measured at 72.5 eV along k_x, the three bands forming the highest valence manifold are labeled VB1, VB2 and VB3, with irreducible band representation Γ_7, Γ_6 and Γ_7. (g) ARPES image made by energy distribution curves collected at Γ for photon energies between 50 and 86 eV.

method known to yield large crack-free crystals [21]. Polycrystalline $CdGeAs_2$ is first synthesized by solid-state reaction: stoichiometric amounts of 4N purity Cd (chunk), Ge (slug), and As (slug) are sealed under high vacuum in a carbon-coated quartz ampule. The mixture is heated at 550°C and 650°C for 24 hours, with intermediate grinding in an argon-filled glove box. For crystal growth, the powders are mixed with $2\,\mu\text{l/cm}^3$ of liquid bromine and sealed in a 40 cm-long quartz ampule at an internal pressure of $\sim 10^{-1}$ Pa. The charge and growth ends of the ampule are placed in a horizontal two-zone furnace held at 675 °C and 650 °C, respectively, for 200 hours. After growth, the furnace is cooled to room temperature at 2 °C/min, and single crystals are collected from the growth end of the ampule.

Like other ternary chalcopyrites, $CdGeAs_2$ crystallizes in space group $I\bar{4}2d$ (No. 122), with body-centered tetragonal symmetry and lattice parameters $a = 5.94$ Å and $c = 11.21$ Å, giving a tetragonal distortion $c/a = 1.89$ [21]. Figure 1(b) shows the conventional tetragonal cell comprising four formula units: Cd (yellow) and Ge (red) lie on the four-

fold axis, while As (blue-green) sits on the twofold axis. The structure is diamond-like, with atoms adopting sp^3 hybridization and tetrahedral coordination: each Cd and Ge atom is bonded to four As atoms, and each As atom is coordinated by two Cd and two Ge cations [22].

ARPES measurements are performed at the APE-LE beamline of the Elettra synchrotron (Trieste), using a Scienta DA30 electron analyzer equipped with electrostatic deflecting lenses to acquire angular maps without moving the sample. Linear horizontal and vertical polarizations are used in the photon-energy range of 50–86 eV to probe the three-dimensional dispersion of bulk bands. The angular resolution is 0.5° and the combined energy resolution (beamline + analyzer) is 30 meV. Samples are cooled to 130 K, providing a good compromise between enhanced spectral quality and minimal charging effects. Thermal and electrical contact is ensured with conductive silver epoxy. The zero of the energy scale is referenced to the Fermi level (E_F) measured on polycrystalline silver in electrical contact with the sample.

The spin-to-charge conversion properties of $CdGeAs_2$ are studied using optical orientation [23–25], a technique in which circularly polarized light excites spin-polarized electrons in the conduction band through dipole-allowed optical transitions. As the injected spins diffuse, they undergo spin-dependent scattering, generating an electromotive field through the inverse spin Hall effect (ISHE) [26]. In this process, the spin current density $\mathbf{j}_s$ is converted into a transverse charge current $\mathbf{j}_c$ according to:

$$\mathbf{j}_c = \gamma\, \mathbf{j}_s \times \mathbf{u}_p, \tag{1}$$

where γ is the spin Hall angle, quantifying the efficiency of the ISHE, and $\mathbf{u}_p$ is the unit vector of the injected degree of spin polarization vector $\mathbf{P}$. The ISHE voltage ΔV_{ISHE} is measured across two Ti(7 nm)/Au(200 nm) electrodes evaporated at the edges of a $4 \times 2 \times 1$ mm^3 $CdGeAs_2$ sample [Fig. 1(c)].

The excitation source is a monochromatized supercontinuum laser (SuperK FIANIUM FIR-20, NKT Photonics) covering the 0.65–1.15 eV photon-energy range with a typical bandwidth of ∼10 meV. A double-modulation scheme is employed: the circular polarization of the light is modulated at 50 kHz by a photoelastic modulator (PEM), while the beam intensity is modulated at 23 Hz by a mechanical chopper. The laser beam is focused onto the sample at a polar angle ϑ with respect to the sample normal in the xz-plane [Fig. 1(c)], using an off-axis configuration with a 0.65 numerical-aperture objective [27, 28]. The optically generated spin current $\mathbf{j}_s$ propagates along the z axis [27], while the ISHE-induced voltage drop ΔV_{ISHE} is measured along y across the Ti/Au contacts. Under these conditions, only the x-axis component of $\mathbf{P}$ satisfies the ISHE geometry of Eq. (1) and can be detected. The signal is demodulated using two lock-in amplifiers in cascade, tuned to the PEM and chopper frequencies, respectively. All ISHE measurements are performed at room temperature.

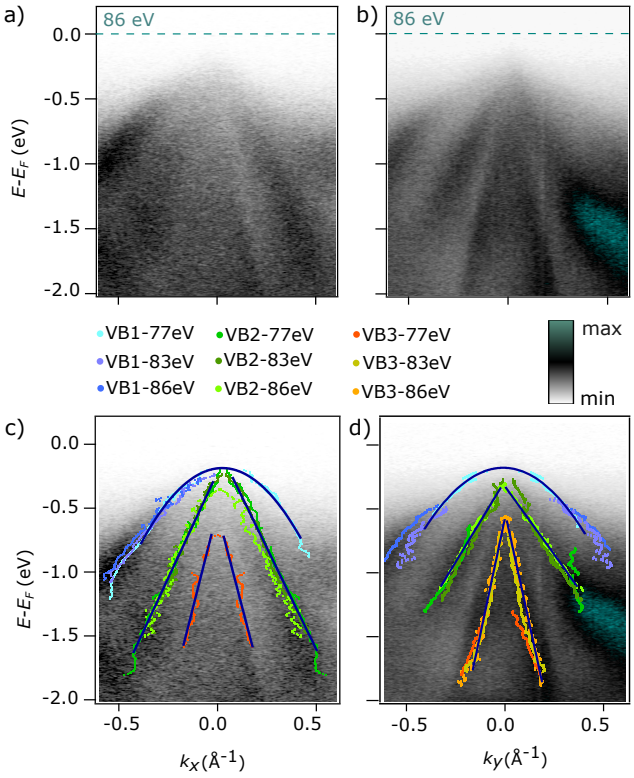

FIG. 2 (a) and (b) band structure measured with a photon energy of 86 eV along k_x and k_y, respectively. (c) and (d) same band dispersions with colored markers to indicate the position of the peaks extracted from the analysis of the momentum distribution curves (MDCs) integrated within a window of 25 meV between -1.75 and -0.25 eV. Different colors correspond to the dataset at 77 eV, 83 eV and 86 eV. The position of the bands is obtained from a fit of the MDC with multiple Lorentzian functions and a polynomial background. Dark-blue lines indicate the best fit of the peaks dispersion: VB1 is well accounted for by a parabolic dispersion, whereas VB2 and VB3 exhibit linear dispersion with large band velocities, comparable to those reported in graphene and in Dirac semimetal candidates.

III. RESULTS AND DISCUSSION

ARPES requires atomically clean surfaces, obtained by post-cleavage in ultra-high vacuum. The crystal structure of $CdGeAs_2$ consists of As and Cd–Ge layers alternating along the [100] and [001] directions of the conventional cell, and it does not exhibit a single preferential cleavage plane. Crystals are generally prismatic and elongated along [111], naturally exposing optically smooth (112), (101), and (011) faces [21]. By fracturing more than twenty crystals, we observed band dispersion only from the (112) termination, with a success rate of $\sim$ 20%.

In reciprocal space, the periodicity is more conveniently described in terms of the body-centered tetragonal

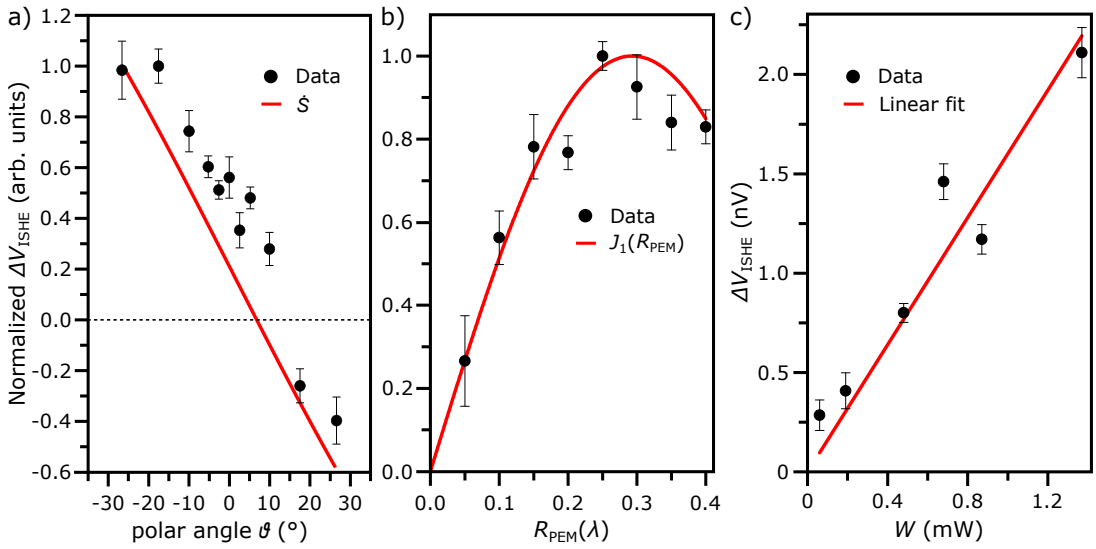

FIG. 3 (a) ΔV_{ISHE} signal normalized to its maximum value as a function of the polar angle ϑ, for $h\nu = 0.8$ eV, $R_{\mathrm{PEM}} = 0.3\lambda$ and $W = 1.37$ mW. This is compared with the spin injection rate $\dot{S}$ in Eq. 4 corresponding to the solid red line, estimated from the 8-band $\mathbf{k}\cdot\mathbf{p}$ model for the geometry of Fig. 1(c). (b) Dependence of ΔV_{ISHE} upon the PEM retardation R_{PEM}, for $h\nu = 0.8$ eV, $\vartheta = -27°$ and $W = 1.37$ mW. The solid red line represents the Bessel function of the first order $J_1(\lambda)$, which describes the dependence of the light circular polarization upon the PEM retardation R_{PEM}. (c) ΔV_{ISHE} as a function of the light incident power W, for $h\nu = 0.8$ eV, $R_{\mathrm{PEM}} = 0.3\,\lambda$ and $\vartheta = -27°$. The straight red line represents a linear fit of the data.

unit cell, which has half the volume of the conventional cell, *i.e.* two formula units. The primitive lattice vectors are $\mathbf{a}_1 = (\mathrm{a}/2, -\mathrm{a}/2, \mathrm{c}/2)$, $\mathbf{a}_2 = (\mathrm{a}/2, \mathrm{a}/2, \mathrm{c}/2)$, and $\mathbf{a}_3 = (-\mathrm{a}/2, -\mathrm{a}/2, \mathrm{c}/2)$. Figure 1(d) shows the corresponding Brillouin zone (BZ); the colored area marks the plane parallel to the surface termination. Labels denote the high-symmetry points as well as the notation adopted in this work for the three components of the electron wave vector. We note that k_{y} and k_{z} are parallel to low-symmetry directions, whereas k_{x} is parallel to ΓX. Figure 1(e) displays a constant-energy map at $E - E_{\mathrm{F}} = -200$ meV measured with 72.5 eV photons. The valence-band maxima form pockets centered at Γ and Γ′, confirming the sample alignment. Strong matrix element effects are responsible for the lack of spectral weight in the Brillouin zone at negative k_{x} values.

Figure 1(f) shows the band dispersion along k_{x} at 72.5 eV photon energy. Three distinct states are resolved at the top of the valence band manifold. No evidence of an inverted band gap is found, consistent with hybrid functional calculations that include electronic correlations beyond the local density approximation [29]. In contrast, local-density-based calculations incorrectly predict a topological insulating phase [30]. The lower edge of the gap (VB1, irreducible representation Γ_7) corresponds to a singlet state that is nearly degenerate and may accidentally intersect with the heavy-hole band (VB2, Γ_6), owing to their different irreducible representations [31]. Experimentally, we confirm the splitting between VB2 and the light-hole band (VB3, Γ_7), induced by the tetragonal crystal field. The splitting of the spin degeneracy under the breaking of inversion symmetry cannot be fully resolved because of band broadening (see, *e.g.*, the arrow at VB2 for negative k_{x}). This broadening is not limited by energy resolution but arises from k_{z} integration due to the surface sensitivity of ARPES and the bulk character of the bands. The dispersion of the bands in the k_{z} direction, orthogonal to the sample surface, is illustrated in Fig. 1(g), which shows energy distribution curves integrated at Γ as a function of the incoming photon energy. We observe the evolution of the upper valence band (VB1), which exhibits a clear parabolic behavior, reaching its maximum for photon energies in the 77-86 eV range. For a value of the inner potential $V_0 = 10$ eV, these energies fall close to the bulk Γ point at $k_{\mathrm{z}} = 4.7$ Å^{-1} [32].

Figure 2(a,b) display dispersions along k_{x} and k_{y}, respectively, measured at 86 eV photon energy. To quantify the band dispersion, we extract momentum distribution curves (MDCs) integrated within a 25 meV window between $E - E_{\mathrm{F}} = -1.75$ and -0.25 eV. Each MDC is fitted with a model including a variable number of Lorentzian peaks on top of a quadratic background, and markers in Fig. 2 report the central position of each peak. The same analysis is repeated for photon energies of 77 eV and 83 eV with the results shown in Fig. 2(c,d). Markers of different colors denote VB1, VB2 and VB3 for the different photon energies along k_{x} [Fig. 2(c)] and k_{y} [Fig. 2(d)]. The near-overlap of markers at different photon energies indicates that the valence bands exhibit only weak out-of-plane dispersion in this energy window, in agreement with Fig. 1(g). Dark-blue lines indicate the best fit of the peaks dispersion.

Both VB2 and VB3 display nearly linear dispersion over an energy range exceeding 1 eV, whereas VB1 is significantly flatter and well described by a parabolic dispersion. A linear fit yields velocities for VB3 ranging from $\sim 0.9 \times 10^6$ m/s along k_x to $\sim 1.3 \times 10^6$ m/s along k_y. For VB2, the velocities are about a factor of two smaller, $\sim 0.5 \times 10^6$ m/s along both k_x and k_y. These values are large and comparable to those reported in graphene [33] and in Dirac semimetals such as Cd_3As_2 [34, 35], Na_3Bi [36], and $ZrTe_5$ [37, 38]. In contrast, VB1 yields effective masses of $\sim 1.09\ m_e$ and $\sim 1.06\, m_e$ along k_x and k_y, respectively. The close agreement of velocities and masses along the two directions highlights the isotropic character of the valence band on the investigated cleave plane.

The characterization of the band structure by ARPES provides crucial information about the electronic states and their parameters, key to understanding the spin–to-charge conversion in $CdGeAs_2$, investigated here through optical spin injection and detection of the ISHE. In the investigated sample [Fig. 1(c)], the x and y axes form an angle $\eta \simeq 37°$ with respect to the crystallographic directions $[1\bar{1}0]$ and $[c/a,\ c/a,\ -a/c]$, expressed in the basis of the direct lattice vectors of the conventional cell [Fig. 1(b)]. The z axis is instead parallel to the [112] direction. As a first step, we verified the consistency of the ISHE signal by measuring its dependence on the polar angle ϑ [Fig. 3(a)], the PEM retardation $R_{\rm PEM}$ in unit of the wavelength λ [Fig. 3(b)], and the incident optical power W [Fig. 3(c)], for photon energy $h\nu = 0.8$ eV. In Fig. 3(a), the $\Delta V_{\rm ISHE}$ normalized signal is reported as a function of the incidence angle ϑ. This curve is compared with the spin injection rate $\dot{S}$ generated and detected in our geometry. The latter is evaluated modeling the band structure with an 8-band $\mathbf{k}\cdot\mathbf{p}$ Hamiltonian (details in Appendix A). The signal behavior as function of ϑ is nicely captured by the model. Figure 3(b) shows the ISHE signal as a function of $R_{\rm PEM}$, which modulates the degree of circular polarization of the incident beam. The data follow the first-order Bessel function $J_1(\lambda)$ with a maximum near $R_{\rm PEM} \approx 0.3\,\lambda$, consistent with the fact that the PEM retardation determines the degree of circular polarization [25]. Finally, Fig. 3(c) displays $\Delta V_{\rm ISHE}$ as a function of the incident optical power W, showing a linear dependence that reflects the proportionality between injected spin-polarized carriers and incident photon flux. These tests confirm the spin-related origin of the detected voltage.

The photon-energy dependence of $\Delta V_{\rm ISHE}$, normalized to photon flux Φ in the 0.65 - 1.15 eV photon energy range, is presented in Fig. 4 for $R_{\rm PEM} = 0.3\,\lambda$ and $\vartheta = -27°$. The latter corresponds to an angle of $\vartheta_{\rm in} \approx -8.5°$ inside $CdGeAs_2$ which refractive index is $n \approx 3$ [39]. The photon flux is $\Phi = W/[\pi(\mathcal{D}/2)^2 h\nu]$, where $\mathcal{D}$ is the spot diameter on the sample ($\approx 10\ \mu$m) and W varies within 50 and 1500 μW in the explored photon-energy range. A pronounced peak is observed at $h\nu \approx 0.7$ eV, followed by an almost constant signal up to ≈1.15 eV. The ISHE spectrum is governed by three parameters: the light absorption coefficient α, the degree of spin polarization P, and the spin diffusion length L_s [27]. Since the value of L_s for $CdGeAs_2$ has not yet been established, while α and P can be directly evaluated from the electronic band structure, in the following we present how to use the ISHE spectrum to gain insight into L_s. To estimate α and P, we have calculated from the 8-band $\mathbf{k}\cdot\mathbf{p}$ model the carrier injection rate $\dot{n}$ and $\dot{S}$ as functions of the photon energy [40–42] (see Appendix A). The results obtained for the experimental ISHE geometry are presented in Fig. 5(a,b). Then P is derived according to the definition $P = \dot{S}/\dot{n}$ [40, 41], while the absorption coefficient α is related to the carrier injection rate as $\alpha = \dot{n}\, h\nu\, /(2n\, c\, \varepsilon_0)$, with c being the light velocity and ε_0 the vacuum permittivity [43]. The spectral dependence of the calculated α and P values are reported in Fig. 5(c,d), respectively.

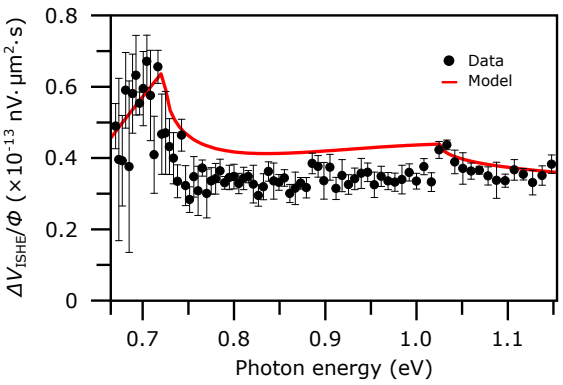

FIG. 4 Photon energy dependence of $\Delta V_{\rm ISHE}$, normalized to the incident photon flux, for $\vartheta = -27°$ and $R_{\rm PEM} = 0.3\,\lambda$. The solid red line shows the spectral dependence obtained from the spin diffusion model described in the text.

Within a one-dimensional spin diffusion model for optically injected carriers (see Appendix B for the derivation) and assuming the spin Hall angle γ as a constant, the normalized ISHE signal follows:

$$\frac{\Delta V_{\rm ISHE}}{\Phi} \propto \frac{P\,\alpha\,L_s^2}{1+\alpha\,L_s}. \qquad (2)$$

At this point, we exploit the calculated parameters P and α to estimate the L_s value, assumed constant, which allows best reproducing the spectral dependence of the ISHE signal. The right side of Eq. (2) is shown in Fig. 5(e) for $L_s = 10\ \mu$m (blue curve), 1 μm (gray) and 100 nm (orange). It is worth noting that the $L_s = 10\ \mu$m curve is representative of the limit $L_s \gg \alpha^{-1}$ of Eq. (2), yielding $\Delta V_{\rm ISHE} \propto P\, L_s$, while th $L_s = 100$ nm curve is representative of the opposite regime $L_s \ll \alpha^{-1}$, yielding $\Delta V_{\rm ISHE} \propto P\,\alpha\, L_s^2$. In the latter case, since $P = \dot{S}/\dot{n}$ and $\alpha \propto \dot{n}$, we get $\Delta V_{\rm ISHE} \propto \dot{S}\, L_s^2$. By comparing the (measured) ISHE spectrum in Fig. 4 and the (computed) $P\,\alpha\, L_s^2\,/\,(1+\alpha\, L_s)$ in the gray shaded area of Fig. 5(e) we observe that the increase of the detected signal up to $h\nu \approx 0.7$ eV is reproduced only by the $L_s = 100$ nm curve. In contrast, the 10 μm curve exhibits a strong de-

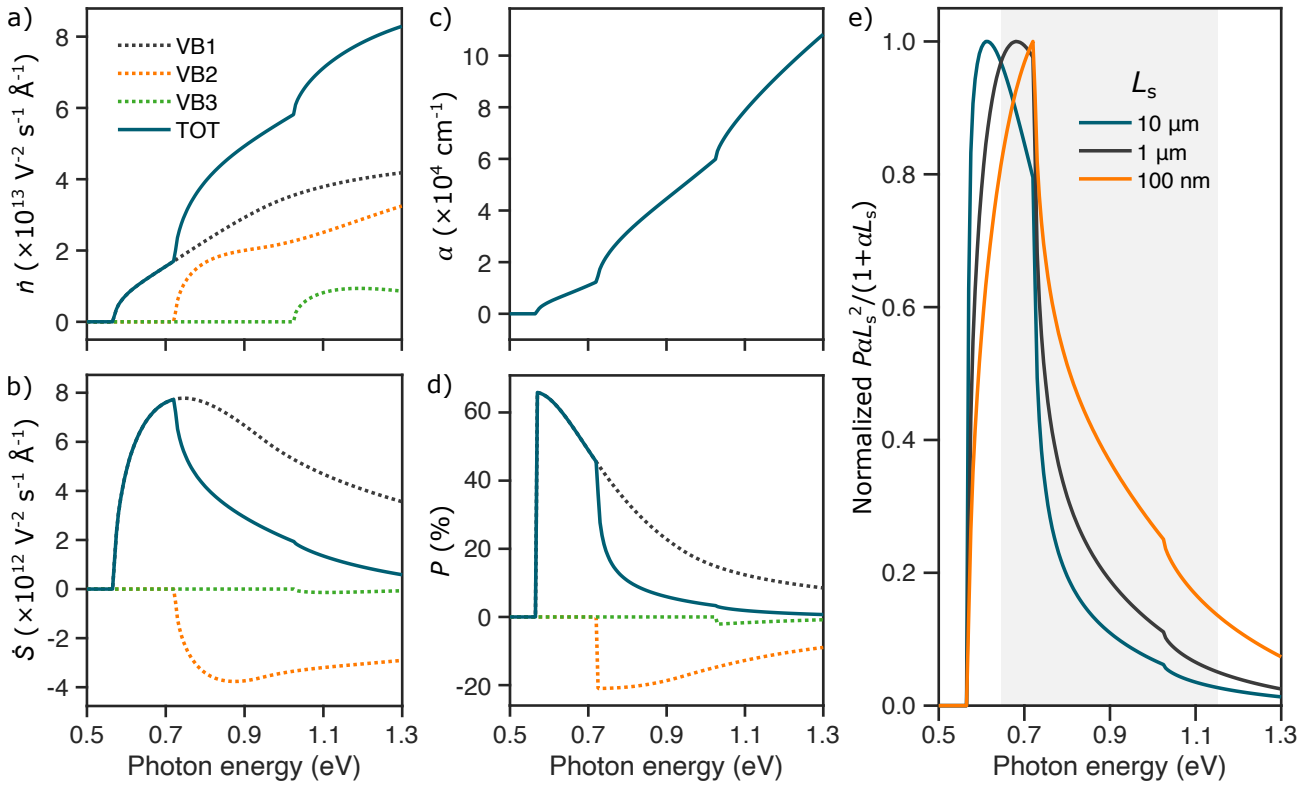

FIG. 5 (a) Carrier injection rate $\dot{n}$, (b) spin injection rate $\dot{S}$, (c) absorption coefficient α, and (d) degree of spin polarization P calculated from the $\mathbf{k}\cdot\mathbf{p}$ model described in Appendix A for direct optical transitions from VB1 (gray dashed line), VB2 (orange dashed line) and VB3 (green dashed line) to the conduction band. The blue line represents the total $\dot{n}$, $\dot{S}$, α, and P, as obtained from the sum of the individual contributions. (e) Photon energy dependence of $P\alpha L_s^2/(1+\alpha L_s)$ evaluated for $L_s = 10$ μm (blue line), 1 μm (gray line), and 100 nm (orange line), with each curve normalized to the maximum. The gray area is the photon energy range of the ISHE spectrum.

crease in the $0.6-0.7$ eV energy range, while the 1 μm remains roughly constant. For $h\nu > 0.7$ eV, all curves feature a sharp decrease due to the onset of transitions from VB2, which have spin polarization opposite to that of VB1 [see Fig. 5(d)]. Nevertheless, the decrease is less pronounced for the $L_s = 100$ nm curve, which, again, better mimics the experimental results [Fig.4]. At higher photon energies, the model for $L_s = 100$ nm predicts a gradual decrease of the signal, not observed experimentally. This discrepancy likely arises from the assumption of constant L_s and γ even when hot electrons are photogenerated well above the conduction-band minimum. Indeed, we already observed that when electrons are photogenerated with a photon energy several hundreds of meV larger than the direct gap, γ increases significantly in semiconductors [27, 28, 44], and this is commonly responsible for enhancing the ISHE signal with increasing photon energy [27, 28]. The spin Hall angle in semiconductors empirically varies with photon energy as $\gamma(h\nu) \propto e^{\mathcal{C}h\nu}$, where $\mathcal{C}$ is a phenomenological parameter. This behavior is observed both in Ge, with $\mathcal{C} \approx 5$ [27], and in GaAs [44], where it is attributed to intervalley scattering of spin-polarized electrons from the Γ valley into the L valley. To account for a similar dependence of the spin-Hall angle also in $CdGeAs_2$, we fit the ISHE spectrum using the results of the previous analysis and an exponential increase of the spin Hall angle with the photon energy. The best fitting parameter is $\mathcal{C} \simeq 3.4$, yielding the ΔV_{ISHE} photon-energy dependence shown in Fig. 4, which nicely reproduces the whole spectrum and especially the nearly flat ISHE response above 0.8 eV. Furthermore, the model partially captures the small peak at ≈ 1.025 eV, which coincides with the absorption onset from VB3. These results point towards an exponential growth of the spin-to-charge conversion efficiency with photon energy also in $CdGeAs_2$. Although spin-polarized holes are optically injected together with spin-polarized electrons, their contribution is neglected in the discussion as the hole spin polarization is expected to vanish much faster than the electron one [45].

Overall, the analysis suggests $L_s \lesssim 100$ nm in $CdGeAs_2$, a value which is comparable to GaAs [46, 47] but much smaller than Si and Ge where $L_s \sim 1$ μm [46, 48–50]. This value is physically consistent with the electronic properties of $CdGeAs_2$, which is characterized by a strong SOC and by the absence of bulk inversion symmetry [12, 51]. As already established for GaAs [52], these two material-specific characteristics result in effective Elliott-Yafet and Dyakonov-Perel spin relaxation mechanisms, which justify the small value of

the spin diffusion length observed in the present study. In the $L_s \ll \alpha^{-1}$ regime applicable to $CdGeAs_2$, $\Delta V_{\rm ISHE} \propto \dot{S}\, L_s^2$, so the small L_s strongly suppresses the ISHE amplitude. Nevertheless, the measured signal is higher than in Ge [27], suggesting a significantly larger γ value for thermalized electrons in $CdGeAs_2$ ($\gamma \sim 10^{-4}$ in Ge [27]). The larger γ value is attributed to more effective spin-to-charge conversion mechanisms that scale with SOC [53]. A precise estimation of γ for $CdGeAs_2$ would require a precise estimation of L_s which is beyond the goal of the present work. It is finally worth mentioning that a short spin diffusion length is the key ingredient to enable fast modulation of spin-dependent signals using high-frequency electric fields, which is promising for spin-based logic applications [47].

IV. CONCLUSIONS

In this work, we have reported, to the best of our knowledge, the first experimental investigation of the electronic band structure of the chalcopyrite semiconductor $CdGeAs_2$ using angle-resolved photoemission spectroscopy and inverse spin Hall effect (ISHE). We resolved three distinct states forming the top of the valence band manifold. Two of them exhibit nearly linear dispersions, with velocities as high as $\sim 1.3 \times 10^6$ m/s (VB3) and $\sim 0.5 \times 10^6$ m/s (VB2), values that are comparable to those reported in graphene and Dirac semimetals such as Cd_3As_2, Na_3Bi, and $ZrTe_5$. The third state (VB1) is significantly flatter and well described by a parabolic dispersion with an effective mass of $\sim 1.1\, m_e$. The close agreement of these parameters along the orthogonal in-plane direction highlights the nearly isotropic character of the valence band within the cleave plane. These results directly validate long-standing theoretical predictions based on the modified Kane model and establish $CdGeAs_2$ as an archetype for studying the coexistence of dispersive and flat bands in chalcopyrite semiconductors.

The band-structure parameters obtained from ARPES provide the basis for interpreting the spin–charge interconversion properties of $CdGeAs_2$, investigated by means of optical spin injection and detection of the ISHE. The ISHE signal exhibits a clear photon-energy dependence, with a pronounced maximum near $h\nu \approx 0.7$ eV followed by a plateau up to ≈ 1.15 eV, in agreement with a model based on an 8-band $\mathbf{k}\cdot\mathbf{p}$ Hamiltonian. The model allowed us to compute carrier and spin injection rates, $\dot{n}$ and $\dot{S}$, as well as the degree of spin polarization $P = \dot{S}/\dot{n}$ and the absorption coefficient α, under experimental conditions. The analysis shows that the normalized ISHE spectrum is mainly governed by VB1→CB transitions up to 0.7 eV, where the onset of VB2 transitions produce a sharp drop of the signal. Comparison with a diffusion model further indicates that the measured voltage scales with $\dot{S}$, leading to $L_s \lesssim 10$ nm in $CdGeAs_2$.

By establishing $CdGeAs_2$ as a semiconductor hosting both high-velocity carriers, efficient optical spin injection and spin-to-charge conversion, this work highlights the potential of chalcopyrites as versatile materials for future opto-spintronics applications.

Appendix A. 8-band *k·p* model

To analyze the ϑ-angle and photon-energy dependencies of the ISHE response, we employed an 8-band $\mathbf{k}\cdot\mathbf{p}$ model to compute the band structure [Fig. 6] and the carrier and spin injection rates [Fig. 5(a,b)] of optically oriented electrons in $CdGeAs_2$. The basis set includes the conduction- and valence-band states $|S\uparrow\rangle$, $|S\downarrow\rangle$, $|X\uparrow\rangle$, $|Y\uparrow\rangle$, $|Z\uparrow\rangle$, $|X\downarrow\rangle$, $|Y\downarrow\rangle$, $|Z\downarrow\rangle$. Remote bands were neglected, since the optical orientation process involves only states near $\mathbf{k} = 0$, where the 8-band approximation is accurate. The Hamiltonian combines the 6×6 valence-band model of Limpijumnong and Lambrecht [51], which includes linear and quadratic coupling terms, with the 8×8 model of Kildal [12] for the conduction band and conduction–valence coupling. The resulting coupling terms are consistent with those found in diamond-like semiconductors [54, 55]. The Hamiltonian, excluding the free-particle kinetic energy, reads

$$H = \begin{pmatrix} E_s & 0 & iPk_x & iPk_y & iPk_z & 0 & 0 & 0 \\ & E_s & 0 & 0 & 0 & iPk_x & iPk_y & iPk_z \\ & & d_1 & -i\Delta_\parallel & e_1 & 0 & 0 & \Delta_\perp \\ & & & d_2 & e_2 & 0 & 0 & -i\Delta_\perp \\ & & & & d_3 & -\Delta_\perp & i\Delta_\perp & 0 \\ & & & & & d_1 & i\Delta_\parallel & e_1 \\ & & & & & & d_2 & e_2 \\ & & & & & & & d_3 \end{pmatrix},$$

with:

$$\begin{aligned} d_1 &= (A_0 + A_2)k_x^2 + B_0 k_y^2 + (B_0 + B_1 + A_1)k_z^2 + \Delta_{\rm c}, \\ d_2 &= (A_0 + A_2)k_y^2 + B_0 k_x^2 + (B_0 + B_1 + A_1)k_z^2 + \Delta_{\rm c}, \\ d_3 &= (A_0 + A_1)k_z^2 + (B_0 + A_2)(k_x^2 + k_y^2), \\ e_1 &= C_0 k_x k_z + iDk_y, \\ e_2 &= C_0 k_y k_z - iDk_x. \end{aligned}$$

The parameters $E_s, \Delta_c, \Delta_\parallel, \Delta_\perp, P, D, A_i, B_i, C_0$ correspond to the energy eigenvalues and spin–orbit splittings at Γ, and linear/quadratic coupling terms. The values were adjusted from Refs. 12 and 51 to account for both earlier reports and the ARPES data presented in this work. The complete parameter set is given in Table I.

Using this Hamiltonian, we computed the carrier injection rate $\dot{n}$ and the spin injection rate $\dot{S}$ as functions of the photon energy for the geometry of Fig. 1(c), following Refs. 40 and 41. Calculations include only spin-dependent direct transitions, evaluated with the linear tetrahedron method [56] over the first Brillouin zone [57], in line with previous works [42, 55]. In particular, we have calculated the matrix elements of the carrier-injection tensor ξ^{aa} and ξ^{cc}, and of the spin-injection pseudotensor ζ^{abc} and ζ^{cab}. Here, the

superscripts refer to Cartesian directions along the axes of the conventional cell [Fig. 1(b)]. In tetragonal systems, the only three nonzero elements in the carrier-injection tensor are $\xi^{aa} = \xi^{bb}$ and ξ^{cc}, and the six nonzero coefficients in the spin-injection pseudotensor are $\zeta^{abc} = \zeta^{bca} = -\zeta^{acb} = -\zeta^{bac}$ and $\zeta^{cab} = -\zeta^{cba}$.

We then computed the spin-injection rate components $\dot{S}_i = \zeta^{ijk} E_j E_k^*$ and the carrier-injection rate $\dot{n} = \xi^{ij} E_i E_j^*$, where the Einstein summation convention over repeated indices is employed. In these expressions, i, j, and k are generic Cartesian directions and E_i is the component along the i-th axis of the electric field of the impinging light. Considering the specific direction of the light wavevector used in the experiments, the carrier-injection rate normalized to the beam intensity can be calculated as

$$\dot{n} = \frac{1}{4}\Big\{3\xi^{aa} + \xi^{cc} + \frac{\xi^{aa} - \xi^{cc}}{\gamma'^2}\Big[\gamma'^2\cos(2\vartheta_{\text{in}}) - 2a^2\cos^2\eta - 2a^2\cos^2\vartheta_{\text{in}}\sin^2\eta + 2a^2\sin^2\vartheta_{\text{in}} - 2ac\sqrt{2}\sin\eta\sin(2\vartheta_{\text{in}})\Big]\Big\}. \quad (3)$$

Furthermore, by considering that the ISHE geometry allows the detection of only the x-axis component of the spin polarization, the spin-injection rate of carriers producing the ISHE signal normalized to the beam intensity assumes the following expression:

$$\dot{S} = \frac{i}{\gamma'^2}\Big[ac\sqrt{2}\big(\zeta^{abc} - \zeta^{cab}\big)\cos\vartheta_{\text{in}}\sin\eta + \gamma'^2\zeta^{abc}\sin\vartheta_{\text{in}} + a^2\big(\zeta^{cab} - \zeta^{abc}\big)\sin\vartheta_{\text{in}}\sin^2\eta\Big]. \quad (4)$$

Here, $\gamma' = \sqrt{2c^2 + a^2}$. Eq. 4 is used to reproduce the ϑ-angle dependence of ΔV_{ISHE} [Fig. 3(a)], and both expressions are employed to compute the photon energy dependence of α and P [Fig. 5(c,d)]. It is worth noting that, unlike materials with cubic symmetry, the directions of the light wavevector and spin-polarization unit vector do not lie in general along the same axis, leading to a nonzero ISHE signal even at normal incidence on the sample surface, as shown in Fig. 3(a).

Appendix B. Spectral dependence of ISHE signal

From Eq. (1), and considering the experimental configuration shown in Fig. 1(c), we obtain $j_{\text{c}}(z) = \gamma\, j_{\text{s}}^x(z)$, where $j_{\text{s}}^x(z)$ is the spin current density flowing along the z axis and polarized along the x axis of Fig. 1(c). Accordingly, the ISHE voltage drop can be expressed as [27]:

$$\Delta V_{\text{ISHE}} = \gamma\, \langle j_{\text{s}}^x(z)\rangle_z\, \rho\, d\,, \quad (5)$$

where ρ is the electrical resistivity, d the distance between the electrodes, and $\langle j_{\text{s}}^x(z)\rangle_z$ denotes the spatial average of the spin current density along the out-of-plane direction, i.e., the component that contributes to the measurable signal across the electrodes. Within a one-dimensional spin diffusion model, the spin current satisfies:

$$\frac{1}{D_{\text{e}}}\frac{\partial j_{\text{s}}^x(z)}{\partial z} = -\frac{s_x(z)}{L_s^2} + \frac{P\,\alpha\,\Phi_{\text{ph}}\,e^{\alpha z}}{D_{\text{e}}}, \quad (6)$$

where $j_{\text{s}}^x(z) = -D_{\text{e}}\,\partial s_x(z)/\partial z$, $s_x(z)$ is the x-polarized spin density, and D_{e} is the electron diffusion coefficient [27]. Equation (6) is solved under the boundary conditions $j_{\text{s}}^x(0, -t) = 0$, reflecting the absence of spin leakage through the sample surfaces at $z = 0$ and $z = -t$, $-t$ being the position of the bottom one. The average spin current density, $\langle j_{\text{s}}^x(z)\rangle_z$, is obtained by averaging $j_{\text{s}}^x(z)$ over the sample thickness t. In the limit $t \gg L_s$, α^{-1}, it can be approximated as:

$$\langle j_{\text{s}}^x(z)\rangle_z = \Phi\,\frac{P\,\alpha\,L_s^2}{t\,(1 + \alpha L_s)}. \quad (7)$$

Substituting Eq. (7) into Eq. (5), the spectral dependence of the normalized ISHE signal, reported in Fig. 4, can be interpreted as $\Delta V_{\text{ISHE}}/\Phi \propto P\,\alpha\,L_s^2\,/\,(1 + \alpha\,L_s)$.

TABLE I Parameters employed in the 8-band $\mathbf{k}\cdot\mathbf{p}$ model. Note that with respect to Ref. 51 we set another parameter C_1 to zero.

Description	Parameter	Value
Eigenvalue at $k = 0$	E_s	0.6424 eV
Crystal-field splitting at $k = 0$	Δ_c	-0.195 eV
Spin-orbit coupling at $k = 0$	$\Delta_{\parallel}$	0.114 eV
	$\Delta_{\perp}$	0.119 eV
Linear coupling terms	P	6.840 eV· Å
	D	0.252 eV· Å
Quadratic coupling terms	A_0	-17.533 eV· Å^2
	A_1	-2.523 eV· Å^2
	A_2	-0.704 eV· Å^2
	B_0	-6.238 eV· Å^2
	B_1	-6.764 eV· Å^2
	C_0	-18.610 eV· Å^2

Acknowledgements

Correspondence and requests for materials should be addressed to A.C. (alberto.crepaldi@polimi.it).

We acknowledge financial supports from the program 'Next Generation EU' - PNRR- M4C2, investment 1.1 - Fondo PRIN 2022 - under project CRESO, Grant ID 20223X5Z5E; CUP D53D23002110001. We acknowledge funding from the CNR-NSTC (Taiwan) Joint Program 2025/2026 "Tailoring the light-matter interaction in highly anisotropic semiconductors for future optoelectronics applications". N. M.

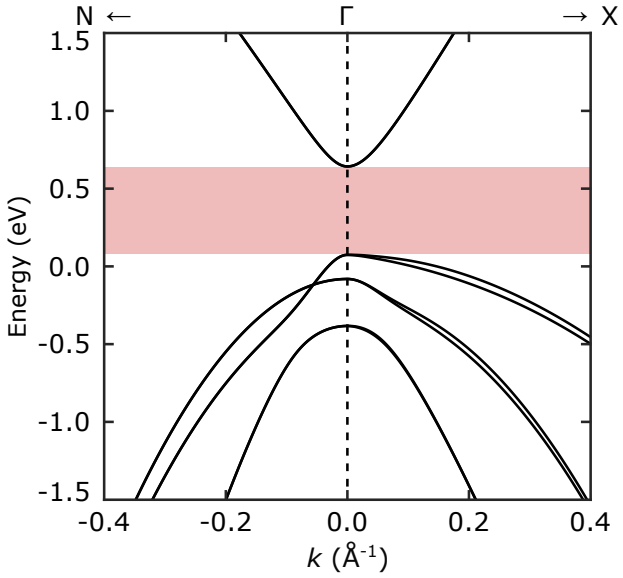

FIG. 6 Bandstructure of $CdGeAs_2$ around the Γ point of the Brillouin zone, calculated by means of a 8-band $\mathbf{k} \cdot \mathbf{p}$ model.

acknowledges financial supports from the program fondo PRIN 2020 - Quantum Transition-metal FLUOrides (QT-FLUO) - ID 20207ZXT4Z - CUP D43C22000360006. N. T. S. acknowledges financial support by the European Union's NextGenerationEU Programme with the I-PHOQS Infrastructure [IR0000016, ID D2B8D520, CUP B53C22001750006] 'Integrated infrastructure initiative in Photonic and Quantum Sciences'. R.S. acknowledges the financial support provided by the Ministry of Science and Technology in Taiwan under Project No. NSTC-114-2124-M-001-003 and No. NSTC-114-2112M001-045-MY3, as well as support from Academia Sinica for the budget of AS-iMATE11412.

This work has been performed in the framework of the Nanoscience Foundry and Fine-Analysis (NFFA-MUR Italy Progetti Internazionali) facility

N. Tarakameh Samani and F. Scali equally contributed to this work.

* E-mail address: alberto.crepaldi@polimi.it

[1] M. L. C. et al., *Electronic Structure and Optical Properties of Semiconductors* (1988).
[2] W. Feng, D. Xiao, J. Ding, and Y. Yao, Phys. Rev. Lett. **106**, 016402 (2011).
[3] V. L. Shaposhnikov, A. V. Krivosheeva, V. E. Borisenko, J.-L. Lazzari, and F. A. d'Avitaya, Phys. Rev. B **85**, 205201 (2012).
[4] D. Parker and D. J. Singh, Phys. Rev. B **85**, 125209 (2012).
[5] J. Ruan, S.-K. Jian, D. Zhang, H. Yao, H. Zhang, S.-C. Zhang, and D. Xing1, Phys. Rev. Lett. **116**, 226801 (2016).
[6] A. Chirilá, P. Reinhard, F. Pianezzi, P. Bloesch, A. R. Uhl, C. Fella, L. Kranz, D. Keller, C. Gretener, H. Hagendorfer, et al., Nat. Mater. **12**, 1107 (2013).
[7] S. Siebentritt, Current Opinion in Green and Sustainable Chemistry **4**, 1 (2017).
[8] B. Sadhukhan, Y. Zhang, R. Ray, and J. van den Brink, Phys. Rev. Mater. **4**, 064602 (2020).
[9] M. Rudysh, M. Piasecki, G. Myronchuk, P. Shchepanskyi, V. Stadnyk, O. Onufriv, and M. Brik, Infrared Phys. Technol. **111**, 103476 (2020).
[10] P. Zürcher and F. Meier, J. Appl. Phys. **50**, 3687 (1979).
[11] E. O. Kane, J. Phys. Chem. Solids. **1**, 249 (1957).
[12] H. Kildal, Phys. Rev. B **10**, 5082 (1974).
[13] M. Orlita, D. M. Basko, M. S. Zholudev, F. Teppe, W. Knap, V. I. Gavrilenko, N. N. Mikhailov, S. A. Dvoretskii, P. Neugebauer, C. Faugeras, et al., Nat. Phys. **10**, 233 (2014).
[14] A. Akrap, M. Hakl, S. Tchoumakov, I. Crassee, J. Kuba, M. O. Goerbig, C. C. Homes, O. Caha, J. Novák, F. Teppe, et al., Phys. Rev. Lett. **117**, 136401 (2016).
[15] R. Juneja, R. Shinde, and A. K. Singh, The Journal of Physical Chemistry Letters **9**, 2202 (2018), pMID: 29642700, URL https://doi.org/10.1021/acs.jpclett.8b00646.
[16] G. G. G. V. G. Dmitriev and D. N.Nikogosyan, *Handbook of Nonlinear Optical Crystals*, pp. 176–344 (Springer-Verlag, Berlin, 1997).
[17] V. Voeliček, Phys. Status Solidi (b) **67**, 731 (1975).
[18] D. S. Chemla, R. F. Begley, and R. I. Byer, IEEE J. Quantum Electron. **10**, 71 (1974).
[19] S. N. Rashkeev, S. Limpijumnong, and W. R. L. Lambrecht, Phys. Rev. B **59**, 2737 (1999).
[20] K. L. Vodopyanov and P. G. Schunemann, Opt. Lett . **23**, 1096 (1998).
[21] F. P. Baumgartner, M. Lux-Steiner, and E. Bucher, J. Electron. Mater. **19**, 777 (1990).
[22] S. F. Marenkin, V. M. Novotortsev, K. K. Palkina, S. G. Mikhailov, and V. T. Kalinnikov, Inorg. Mater. **40**, 93 (2004).
[23] G. Lampel, Physical Review Letters **20**, 491 (1968).
[24] I. Žutić, J. Fabian, and S. Das Sarma, Rev. Mod. Phys. **76**, 323 (2004).
[25] F. Bottegoni, C. Zucchetti, G. Isella, M. Bollani, M. Finazzi, and F. Ciccacci, La Rivista del Nuovo Cimento **43**, 45 (2020).
[26] E. Saitoh, M. Ueda, H. Miyajima, and G. Tatara, Applied physics letters **88**, 182509 (2006).
[27] C. Zucchetti, F. Bottegoni, G. Isella, M. Finazzi, F. Rortais, C. Vergnaud, J. Widiez, M. Jamet, and F. Ciccacci, Phys. Rev. B **97**, 125203 (2018).
[28] A. Marchionni, C. Zucchetti, F. Ciccacci, M. Finazzi, H. S. Funk, D. Schwarz, M. Oehme, J. Schulze, and F. Bottegoni, Appl. Phys. Lett. **118**, 212402 (2021).
[29] M. Yu, X. Xiao, Z. Xiong, J. Li, X. Liu, W. Huang, B. Chen, and Z. He, Mater. Today Commun. **31**, 103276 (2022).
[30] M. G. Vergniory, L. Elcoro, C. Felser, B. A. B. N. Regnault, and Z. Wang, Nature **566**, 480 (2019).
[31] S. Limpijumnong and W. R. L. Lambrecht, Phys. Rev. B **65**, 165204 (2002).
[32] T. Weber, R. Georgii, and P. Böni, SoftwareX **5**, 121 (2016).
[33] A. Bostwick, T. Ohta, T. Seyller, K. Horn, and E. Rotenberg, Nat. Phys. **3**, 36 (2007).
[34] Z. K. Liu, J. Jiang, B. Zhou, Z. J.Wang, Y. Zhang, H. M.Weng, D. Prabhakaran, S.-K. Mo, P. D. H. Peng an, T. Kim, et al., Nat. Mater. **13**, 677 (2014).
[35] S. Roth, H. Lee, A. Sterzi, M. Zacchigna, A. Politano, R. Sankar, F. C. Chou, G. Di Santo, L. Petaccia, O. V. Yazyev, et al., Phys. Rev. B **97**, 165439 (2018).
[36] Z. K. Liu, B. Zhou, Y. Zhang, Z. J. Wang, H. M. Weng, D. Prabhakaran, S.-K. Mo, Z. X. Shen, Z. Fang, X. Dai, et al., Science

343, 864 (2014).
[37] Q. Li, D. E. Kharzeev, C. Zhang, Y. Huang, I. Pletikosic, A. V. Fedorov, R. D. Zhong, J. A. Schneeloch, G. D. Gu, and T. Valla, Nat. Physics **12**, 550 (2016).
[38] G. Manzoni, A. Sterzi, A. Crepaldi, M. Diego, F. Cilento, M. Zacchigna, P. Bugnon, H. Berger, A. Magrez, M. Grioni, et al., Phys. Rev. Lett. **115**, 207402 (2015).
[39] S. Xue, J. Ning, B. Zhang, Q. Wu, F. Zhang, and W. Zhang, Coatings **12**, 1778 (2022).
[40] F. Nastos, J. Rioux, M. Strimas-Mackey, B. S. Mendoza, and J. Sipe, Physical Review B **76**, 205113 (2007).
[41] J. Rioux and J. Sipe, Physical Review B **81**, 155215 (2010).
[42] F. Scali, M. Finazzi, F. Bottegoni, and C. Zucchetti, arXiv preprint arXiv:2510.09525 (2025).
[43] J. Cheng, J. Rioux, J. Fabian, and J. E. Sipe, Phys. Rev. B **83**, 165211 (2011).
[44] N. Okamoto, H. Kurebayashi, T. Trypiniotis, I. Farrer, D. Ritchie, E. Saitoh, J. Sinova, J. Mašek, T. Jungwirth, and C. Barnes, Nature Materials **13**, 932 (2014).
[45] D. Hilton and C. Tang, Physical Review Letters **89**, 146601 (2002).
[46] F. Bottegoni, C. Zucchetti, G. Isella, E. Pinotti, M. Finazzi, and F. Ciccacci, J. Appl. Phys. **124**, 033902 (2018).
[47] F. Scali, M. Finazzi, F. Bottegoni, and C. Zucchetti, Journal of Applied Physics **137**, 063906 (2025).
[48] C. Zucchetti, F. Bottegoni, C. Vergnaud, F. Ciccacci, G. Isella, L. Ghirardini, M. Celebrano, F. Rortais, A. Ferrari, A. Marty, et al., Phys. Rev. B **96**, 014403 (2017).
[49] C. Zucchetti, F. Scali, P. Grassi, M. Bollani, L. Anzi, G. Isella, M. Finazzi, F. Ciccacci, and F. Bottegoni, APL Mater. **11**, 021102 (2023).
[50] C. Zucchetti, F. Scali, A. Ballabio, M. Bollani, G. Isella, G. Ferrari, M. Finazzi, F. Ciccacci, and F. Bottegoni, Appl. Phys. Lett. **125**, 172404 (2024).
[51] S. Limpijumnong and W. R. Lambrecht, Physical Review B **65**, 165204 (2002).
[52] G. Pikus and A. Titkov, Optical Orientation **8**, 73 (1984).
[53] J. Sinova, S. O. Valenzuela, J. Wunderlich, C. H. Back, and T. Jungwirth, Reviews of modern physics **87**, 1213 (2015).
[54] D. Rideau, M. Feraille, L. Ciampolini, M. Minondo, C. Tavernier, H. Jaouen, and A. Ghetti, Physical Review B—Condensed Matter and Materials Physics **74**, 195208 (2006).
[55] P. Mudi, S. K. Khamari, S. Khan, C. Zucchetti, F. Bottegoni, and T. Sharma, Journal of Physics D: Applied Physics **58**, 015108 (2025).
[56] H. Jeschke, *Computational Methods in Solid State Theory* (2016).
[57] W. Setyawan and S. Curtarolo, Computational materials science **49**, 299 (2010).